

Sensitive Aeromagnetic System for Unexploded Ordnance Detection With High Detection Accuracy and Range

Ying Shen¹, Zhiyue Chen, Junqi Gao², Pengfei Zhang³, and Xiaobao Yang

Abstract—Utilizing a rotor drone equipped with a magnetometer presents a practical solution for rapidly surveying unexploded ordnance (UXO) areas potentially buried underground. This method effectively reduces operational risks and enhances overall efficiency. Our study has developed an aeromagnetic gradient detection system featuring a scalar sensor mounted on a rotor-based unmanned aerial vehicle (UAV). Experimental results affirm the effectiveness of differential processing in mitigating common-mode noise from the carrier platform and in neutralizing the impact of geomagnetic gradients. The system's dynamic noise is $S_i = 0.013$ nT. The wavelet entropy reduction algorithm, utilizing a “sym6” wavelet basis with $j = 4$ wavelet decomposition, increases the low signal-to-noise ratio (SNR) = -0.78 to 8.46 dB, thereby improving the detection of weak magnetic signals. The system's ultimate depth detection capability for eight buried unexploded bombs has been quantified: the H30, with a length of 17 cm and a mass of 0.3 kg, has a maximum detection range of $H = 120$ cm; the 120-mm caliber projectile, with a length of 240 cm and a mass of 25.8 kg, achieves a maximum detection range of $H = 550$ cm. Such detection capability meets practical detection needs. Furthermore, we perform 50 test sets to assess its detection performance, with four types UXOs randomly placed within a 450-m² area. It took 270 s to scan the 450-m² area and 60 s to process data. The system demonstrates a correct detection rate of 94.5% while maintaining a false alarm rate of 2%.

Index Terms—Buried unexploded ordnance, gradient detection system, limit detection indicators, noise suppression, wavelet entropy.

I. INTRODUCTION

AS THE conflict in Ukraine persists, the nation has become the most affected by unexploded ordnance (UXO) worldwide, with more than 173 500 km² area at serious risk. To date, UXO has killed 298 civilians and injured another 632 in Ukraine, profoundly impacting the daily lives and work of the local populace. Employing traditional ground-penetrating radar, a deminer can typically clear 100 m²/day.

Received 15 October 2024; revised 25 December 2024; accepted 7 January 2025. Date of publication 10 January 2025; date of current version 27 January 2025. This work was supported in part by the National Key Research and Development Program of China under Grant 2022YFC3104000, in part by the National Natural Science Foundation Youth Program under Grant 62101151, and in part by the Natural Science Foundation of Heilongjiang Province under Grant YQ2021F001. (Corresponding author: Junqi Gao.)

The authors are with the College of Underwater Acoustic Engineering, Harbin Engineering University, Harbin 150001, China, and also with Qingdao Innovation and Development Base, Harbin Engineering University, Qingdao, Shandong 266400, China (e-mail: shenyinying@hrbeu.edu.cn; 13739211526@hrbeu.edu.cn; gaojunqi@hrbeu.edu.cn; zhangpf9009@hrbeu.edu.cn; jack.yang@hrbeu.edu.cn).

Digital Object Identifier 10.1109/LGRS.2025.3528102

Given the current situation, World Bank estimates that it would take 757 years and \$38 billion to effectively clear Ukraine, assuming the deployment of 500 demining teams [1], [2]. Consequently, it underscores the urgency to address such issue and develop an efficient and safe method for detecting unexploded bombs. Such new scientific-technology progress has to overcome the challenges associated with traditional detection methods [3], [4], including high power consumption, limited detection range, high false alarm rates, and the time-consuming nature of ground-penetrating radar operations [5], [6], [7].

With the rapid development of unmanned aerial vehicle (UAV) technology, airborne magnetic measurement systems have begun to be used in the field of UXO detection [3], [8], [9]. According to ultralow-altitude and fast sweeping, UAV-based magnetic detection systems have significant advantages in terms of detection efficiency and spatial resolution [10]. The autonomous aeromagnetic system developed by vector magnetic sensor (Fluxgate, Bartington) is undesirable for detecting small targets due to the large dynamic noise 500 nT in time domain [11]. In comparison, the aeromagnetic detection system developed by scalar magnetic sensor can reduce dynamic noise significantly. For example, scalar aeromagnetic system based on two cesium optical-pump magnetometers has a dynamic noise of 20 nT in time domain [12]. Currently, the related research focuses on the positioning, tracking, speed estimation, and classification of vehicles or ships. It is still mainly oriented on the target objects with strong magnetism and large volume compared with UXO [13], [14]. Indeed, it still does not solve the problem to detect weak magnetic objects. Scalar aeromagnetic system has a UXO detection range between 1.5 and 2.3 m for bombs weighing between 8.1 and 48.3 kg [9], [15]. Clearly, such detection system is insensitive to accurately find the buried UXO within 5 kg, which is often buried with a depth of 1–2 m.

To address the urgent need for searching covert UXO, a high-sensitive aeromagnetic system is developed with high detection accuracy and range. We employ a semi-rigid damping mechanism to connect two scalar magnetometers with the UAV body. For eight types of UXOs weighing between 0.3 and 25.8 kg, the effective detection distance is significantly improved to be 1–5.5 m. Subsequently, four UXOs were randomly buried in an area of 450 m² to evaluate the system's correct detection rate and false alarm rate for finding the hidden small targets.

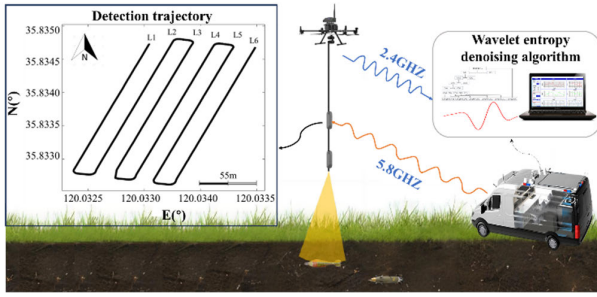


Fig. 1. *TRU100-23* detection schematic. The inset is the detection trajectory.

TABLE I
SYSTEM PERFORMANCE PARAMETERS

Overall performance parameters		Fusion subsystem parameters	
Source	24 V	Transmission mode	Wireless
Power dissipation	8 W	Transmission speed	10 kb/s
Max Gradient Field	300 nT/cm	Positioning accuracy	5 cm
Sensitivity	3 pT/√Hz	Sampling rate	10 Hz

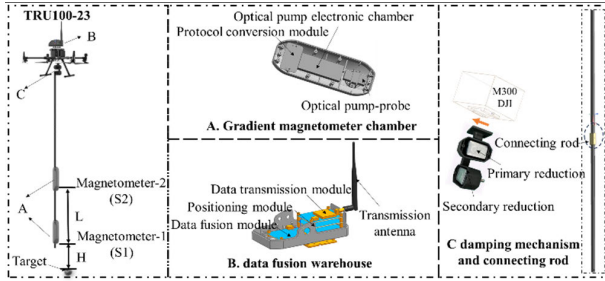


Fig. 2. Hardware components of the *TRU100-23* system.

II. WAVELET ENTROPY DENOISING ALGORITHM

A. System Dynamic Noise

The intelligent aeromagnetic system *TRU100-23* (Tsingtao Haiyuehui Technology Company Ltd., Shandong Province, China) is depicted in Fig. 1, which is designed for searching and identifying the buried UXOs [16].

The basic properties of the *TRU100-23* can be found in Table I. A positioning accuracy of 5 cm is achieved by the real-time kinematic (RTK) to measure tiny objects. The compact rubidium magnetic sensors and a carbon fiber frame add up to be only 1.5 kg, which allows to operate the sensing load even from comparatively small drones. The system operates with an overall power of 8 W, equipped with a 2.4-GHz data transmission module, having the potential to be a new class of aeromagnetic system that are high resolution, lightweight, low power-consuming, and cost-effective.

Fig. 2 illustrates the hardware components, which include a gradient magnetometer (A), a data fusion chamber (B), a damping mechanism, and connecting rod (C). The gradient magnetometer consists of two rubidium optical pumps (S1 and S2), which are spaced $L = 0.5$ -m apart. The detection height (H) measures the distance between S1 and the center of the buried target. The data transmit wirelessly via the transmission module at a rate of 10 kb/s.

The test track with six lines in length of 200 m is shown in Fig. 1 inset for the system's dynamic noise evaluation. The flight altitude is set at $H = 30$ m, with a constant speed $v = 2$ m/s.

TABLE II
DYNAMIC NOISE S_i ASSESSMENT PARAMETERS

	L1	L2	L3	L4	L5	L6	Ave
S_i (nT)	0.010	0.012	0.021	0.011	0.012	0.011	0.013

Following the method described in the technical specification for aeromagnetic measurement [17], the dynamic noise S_i is determined using the formula:

$$S_i = \frac{1}{\sqrt{70}} \sqrt{\frac{1}{n-1} \sum_{i=1}^n (B_i - \bar{B})^2} \quad (1)$$

$$B_i = T_{i-2} - 4T_{i-1} + 6T_i - 4T_{i+1} + T_{i+2} \quad (2)$$

$$\bar{B} = \frac{1}{n} \sum_{i=1}^n B_i \quad (3)$$

where T_i is the magnetic measurement data at point i . B_i is the fourth-order difference of the magnetic measurement data at point i . n is the number of observation points involved in the calculation.

Table II presents the calculation of the dynamic noise evaluation index of the aeromagnetic system according to (1)–(3). The findings demonstrate that the dynamic noise of the system ranges from $0.01 \leq S_i \leq 0.021$ nT, and the overall average is $S_i = 0.013$ nT. It satisfies the technical requirements of the first-level standard $S_i < 0.08$ nT for aeromagnetic specifications.

B. Definition of Wavelet Entropy

We use wavelet entropy denoising to detect UXO magnetic signals in noisy environments for magnetic anomaly detection.

Discrete wavelet transform is performed on the target signal, and the discrete wavelet coefficients at k th moment in the j th layer decomposition scale is written as $C_j(k)$ [18]; then, the total energy of the signal is expressed as

$$E = \sum_j E_j = \sum_j \sum_k |C_j(k)|^2, \quad j = 1, 2, \dots, N. \quad (4)$$

Then, the relative wavelet energy for each layer can be obtained as

$$p_j = \frac{E_j}{E}. \quad (5)$$

Since $\sum_{j=1}^N p_j = 1$, then p_j reflects the energy distribution of the signal at different scales. Combined with information theory, the magnitude of entropy value reflects the uniformity of the probability distribution of the signal. When the probability distribution disorder of the signal is higher, the entropy value is larger and vice versa the entropy value is smaller. We process the wavelet transform coefficient matrix into a probability distribution sequence. The entropy value calculated from this sequence indicates the orderliness of the signal's probability distribution [19]. Thus, the wavelet entropy P_{WT} corresponding to layer j , which can be expressed as

$$P_{WT} = - \sum_j p_j \ln(p_j). \quad (6)$$

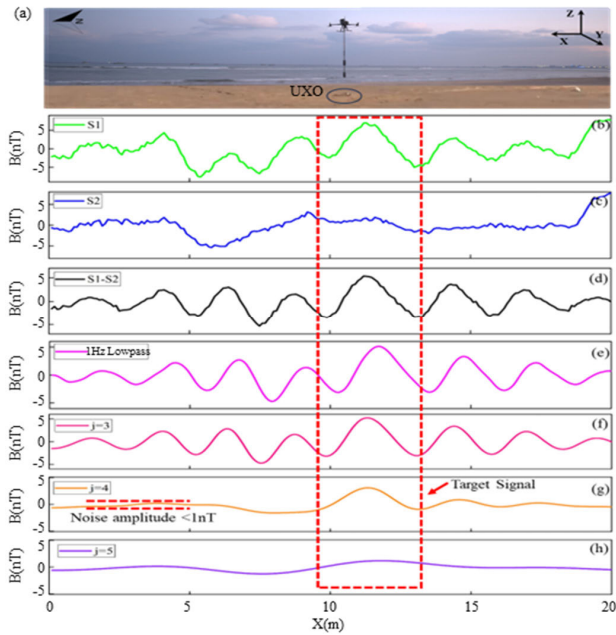


Fig. 3. Detection scenarios and data processing. (a) Scenes, (b) $S1$, (c) $S2$, (d) $S1-S2$, (e) 1-Hz low pass, (f) wavelet decomposition of $j = 3$, (g) wavelet decomposition of $j = 4$, and (h) wavelet decomposition of $j = 5$.

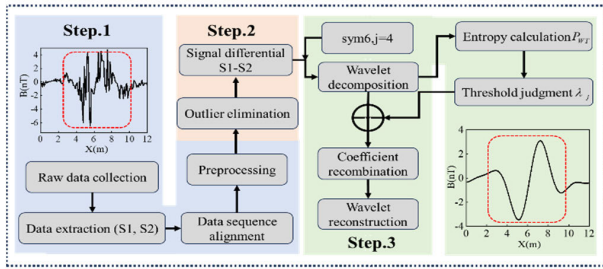


Fig. 4. Wavelet entropy noise reduction algorithm process.

C. Threshold Determination

The noise is mainly concentrated in the intervals with larger wavelet entropy values, which can be assumed that the wavelet coefficients in this subinterval are caused by noise. Therefore, the wavelet entropy of each decomposition layer is analyzed. The average of the wavelet coefficients σ_j exhibiting the highest wavelet entropy is utilized as the noise variance for each scale layer. Then, the threshold values for each layer can be obtained as [20]

$$\lambda_j = \sigma_j \sqrt{2 \log(N)} \quad (7)$$

where $\sigma_j = \text{median}(d_{j, \max}(P_{WT}))/0.6745$.

Equation (7) indicates that coefficients below the thresholds λ_i in each decomposition layer are set to zero.

D. Determination of Optimal Wavelet Layers

The test data, captured at a flight altitude of $H = 120$ cm and velocity of $v = 1.5$ m/s, are shown in Fig. 3(a). The flying UAV's own electromagnetic and altitude interferences seriously drown the weak target signal. The signal-to-noise ratios (SNRs) for $S1$ and $S2$ were only $\text{SNR} = -0.95$ dB and $\text{SNR} = -1.3$ dB, respectively, as shown in Fig. 4(b) and (c). The SNR of $(S1-S2)$ is modestly improved to $\text{SNR} = -0.78$ dB, but the target signal remains hard to discern,

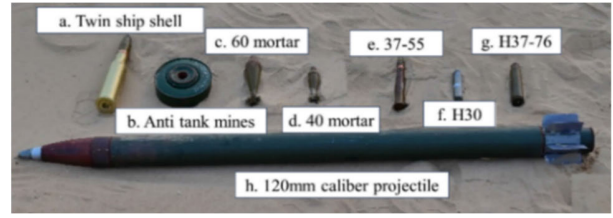


Fig. 5. Picture of eight types of UXO.

as shown in Fig. 3(d). A low-pass filter of 1 Hz also fails to extract the target signal, as shown in Fig. 3(e). In order to determine the optimal number of decomposition layers in the wavelet entropy algorithm. For the reconstructed signals, SNRs are improved to be $\text{SNR} = 0.21, 8.46,$ and 4.63 dB for levels $j = 3, 4,$ and 5 respectively, as shown in Fig. 3(f)–(h).

It reveals that a decomposition level of $j = 3$ fails to sufficiently suppress high-frequency noise components due to its lower level, as shown in Fig. 3(f). For $j = 5$, noise is attenuated while valuable signal components are lost, resulting in a marked reduction in signal amplitude and broadening of wave width. This level also introduces more signal distortion with an increase in decomposition layers, as shown in Fig. 3(h). At the decomposition level $j = 4$, noise is kept below 1 nT. The signal retains its amplitude and bandwidth, as shown in Fig. 3(g). Consequently, for optimal SNR enhancement and signal integrity, the preferred number of wavelet decomposition layers is $j = 4$.

A schematic flowchart of obtaining magnetic signals by wavelet entropy denoising is illustrated in Fig. 4, which comprises three steps. First, extract the raw data of $S1$ and $S2$ acquired by the *TRU100-23* aeromagnetic system and preprocess the data such as alignment. The second step is to eliminate the dead zones in the $S1$ and $S2$ data, which are caused by system steering and violent oscillations and then differential processing to eliminate the effect of common-mode noise. The last step is to obtain wavelet coefficients of each layer by performing a four-layer wavelet decomposition of differential data based on the “*sym6*” wavelet basis function. The signal is reconstructed according to the wavelet coefficient that satisfies the threshold after filtering to achieve noise suppression.

III. METHODS AND RESULTS OF DETECTION OF MAGNETIC ANOMALIES IN BURIED TARGETS

This study aims to the detection, localization, and identification of eight prevalent types of unexploded ordnance using the wavelet entropy denoising algorithm.

A. Detection Depth Analysis

As shown in Fig. 5, the eight types of unexploded ordnance include *twin ship shells*, *anti-tank mines*, *60 mortar*, *40 mortar*, *37-55*, *H30*, *H37-76*, and *120-mm caliber shells*. The specific parameters of the UXO are summarized in Table III. The testing site is located at Naval Park in Qingdao, with clear weather conditions, summer temperatures of 24 °C, and southwest winds of levels 2 and 3. The speed is set to $v = 1.5$ m/s. A wavelet noise reduction algorithm based on the “*sym6*” wavelet basis with $j = 4$ layers is used to carry out

TABLE III
SUMMARY OF TEST RESULTS

Target	Weight (kg)	Length (cm)	Limit H(cm)	B (nT)
a <i>Twin ship shell</i>	4.9	53	150	5
b <i>Anti tank mines</i>	2.3	28	150	3
c <i>60 mortar</i>	2.9	30	150	4
d <i>40 mortar</i>	1.2	24	120	4
e <i>37-55</i>	1.2	38	120	6.5
f <i>H30</i>	0.3	17	120	3.5
g <i>H37-76</i>	0.7	24	100	2.5
h <i>120mm caliber projectile</i>	25.8	240	550	7

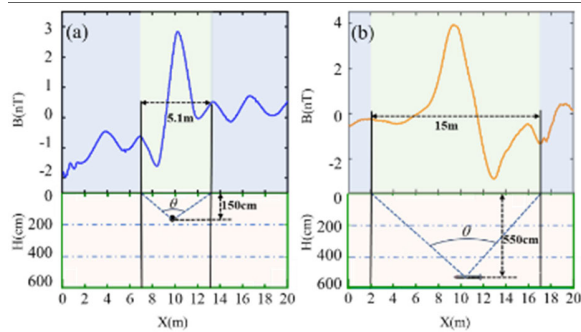


Fig. 6. Comparison of Test Signals. (a) Twin ship shell signals. (b) Anti tank mines signals.

a study on the pulling capability of eight unexploded ordnance aeromagnetic detection limit depths.

The detection parameters for the eight types of unexploded ordnance are summarized in Table III. The detection limit for the *twin ship shell* is $H = 150$ cm, with a target magnetic anomaly signal amplitude of $B = 5$ nT. The detection limit for the *anti-tank mines* is $H = 150$ cm, with a target signal amplitude of $B = 3$ nT. Similarly, the detection limit for the *60 mortar* is $H = 150$ cm, with a target signal amplitude of $B = 4$ nT. The detection limit for the *40 mortar* is $H = 120$ cm, with a signal amplitude of $B = 4$ nT. The detection limit for the *37-55* is $H = 120$ cm, with a target amplitude of $B = 6.5$ nT. For *H30*, the limit is $H = 120$ cm, with a target amplitude of $B = 3.5$ nT, whereas the detection limit for the *H37-76* is $H = 100$ cm, with a target amplitude of $B = 2.5$ nT. Finally, the detection limit for the 120-mm caliber shell is $H = 550$ cm, with a target amplitude of $B = 7$ nT.

As shown in Fig. 6(a), the *twin ship shell* exhibits a limit depth of $H = 150$ cm, with a continuous path of the signal wave width spanning approximately 5.1 m. To verify the efficacy of the wavelet entropy denoising algorithm, it is crucial to ensure that $\theta \in [90, 130]$ satisfies the condition, where the effective range of the sustained path of magnetic anomaly signals is less than $2\sqrt{3}$ closed path approach (CPA) [21]. As shown in Fig. 6(b), the limit depth of the 120-mm caliber shell is $H = 550$ cm, and the span of the continuous path of the signal wave width is 15 m. The results underscore the substantial difference in the wave width of the magnetic anomaly curves among unexploded ordnance with significant variations in size.

The results demonstrate the capability of this technology to detect various types of unexploded ordnance at distances

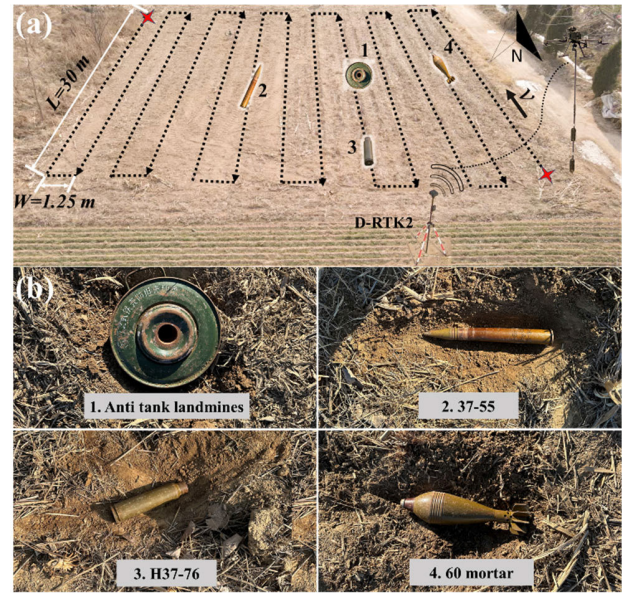


Fig. 7. System-relevant probability detection scenarios and target objects. (a) TP rate testing site for target identification. (b) Target objects.

exceeding 100 cm. Notably, the 0.3-kg *H30* with a length of 17 cm is detected up to 120 cm with a signal of $B = 3.5$ nT. In practical scenarios, the burial depth of unexploded ordnance within the target range typically does not exceed 20 cm. Considering the influence of surface vegetation coverage, achieving a detection capability exceeding 100 cm through the application of ultralow-altitude aeromagnetic detection technology fulfills practical requirements.

B. Target Recognition Analysis

The target recognition capability is assessed in Wangjiagang Village, Huangdao District, Qingdao City ($N = 35.8545^\circ$ and $E = 119.9429^\circ$), over a scanning area of 450 m^2 comprising 13 measurement lines. Each line is 30 m long and 1.25 m wide. The aeromagnetic system received real-time differential positioning data from the *D-RTK2* base station. Weather conditions were clear with a temperature of 4°C and wind speeds at level 3.

Fig. 7(a) illustrates the evaluation tests for the true positive (TP) rate and true negative (TN) rate of target recognition. Four kinds of UXO were randomly deployed: 2.3-kg *anti-tank mines*, 1.2-kg *37-55*, 0.7-kg *H37-76*, and 2.9-kg *60 mortar*. The 60 mortars were buried at a depth of 10 cm, the anti-tank mines at 20 cm, and the other two ammunitions at 15 cm. Wind speed and terrain fluctuations may introduce errors in the actual test altitude. Under the same testing conditions, out of the 200 samples from 50 sets each containing four types of unexploded ordnance, 189 were “true (T)” corresponding to “detection result positive (P).” In 11 cases, “the real situation true (T)” matched “the detection result negative (N).” Thus, from the 50 scanning sets, the correct detection rate is $TP = 94.5\%$, and the false nondetection rate is $TN = 5.5\%$. The target recognition outcomes are detailed in Table IV. It represents a significant TP enhancement over previous airborne ground-penetrating radar with a correct detection rate of $TP = 80\%$, as it is susceptible to soil conditions [5].

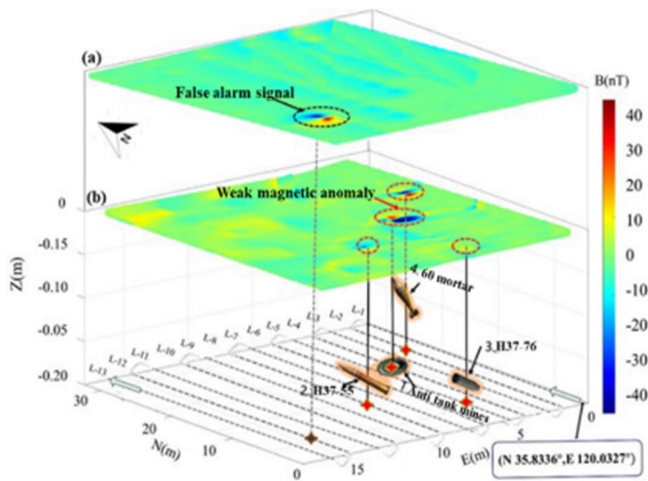


Fig. 8. Overall observation map of the side-scan area. (a) Target-free area. (b) Arrange targets.

TABLE IV

RESULTS OF THE MAGNETIC SURVEY FOR 50 SETS OF BURIED UNEXPLODED ORDNANCE OF FOUR TYPES

Fact	Results	Positive		Negative	
		number		number	
True		number	189	number	11
		TP	94.5%	TN	5.5%
False		number	1	number	49
		FP	2%	FN	98%

The false positive (FP) rate and the false negative (FN) rate for target recognition were evaluated. In a target-free area, the drone performed 50 scanning measurements at $v = 1.5$ m/s and an altitude of $H = 50$ cm. Out of these, 49 cases of “the real situation is false (F)” matched “the detection result is negative (N),” and one case of “the real situation is false (F)” matched “the detection result is positive (P).” Hence, from 50 scanning operations, the false negative rate is $FN = 98\%$ and the false positive rate is $FP = 2\%$. These false alarms could stem from the drone’s unstable flight caused by wind or the pilot’s inconsistent acceleration and deceleration. The single 2-D magnetic contour map is shown in Fig. 8(a).

In addition, Fig. 8(b) presents the magnetic imaging results for target recognition. The magnetic anomaly signal amplitude from the *60 mortar* at a detection distance of $H = 60$ cm is $B = 70$ nT. This is in contrast to the magnetic signal of $B = 4$ nT at $H = 150$ cm, as noted in Table III. The results conform to the inverse-cube law of magnetic dipole attenuation, which corroborates the system’s stability and reliability.

IV. CONCLUSION

A wavelet entropy denoising algorithm is incorporated into the gradient magnetic anomaly detection system, which integrates with UAV. The algorithm successfully mitigates noise from the moving platform and the background field in actual UXO scanning scenarios. It accurately extracts the target signal even at low SNR, while maintaining signal integrity. The distinct differences in wave width between the magnetic anomaly curves of *twin ship* and *120-mm caliber shells* facilitate future classification of unexploded ordnance based on time–frequency signal characteristics. System testing across diverse conditions has proven its effectiveness in detecting

buried ordnance and its capability for complex tasks. The system has achieved a correct detection rate of $TP = 94.5\%$ and a false alarm rate of $FP = 2\%$.

REFERENCES

- [1] *Ukraine Rapid Damage and Needs Assessment*, World Bank, Government Ukraine, Eur. Commission, Washington, DC, USA, Aug. 2022.
- [2] K. Nieczydor, “Ukraine: The world’s biggest minefield,” OSW Commentary, Centre Eastern Studies, Nov. 2023. [Online]. Available: <https://www.osw.waw.pl/en/publikacje/osw-commentary/2023-11-22/ukraine-worlds-biggest-minefield>
- [3] Z. Qi, X. Li, H. Li, and W. Liu, “First results from drone-based transient electromagnetic survey to map and detect unexploded ordnance,” *IEEE Geosci. Remote Sens. Lett.*, vol. 17, no. 12, pp. 2055–2059, Dec. 2020.
- [4] W. E. Doll et al., “Historical development and performance of airborne magnetic and electromagnetic systems for mapping and detection of unexploded ordnance,” *J. Environ. Eng. Geophys.*, vol. 17, no. 1, pp. 1–17, Mar. 2012.
- [5] M. Garcia-Fernández, G. Álvarez-Narciandi, Y. Álvarez López, and F. Las-Heras Andrés, “Improvements in GPR-SAR imaging focusing and detection capabilities of UAV-mounted GPR systems,” *ISPRS J. Photogramm. Remote Sens.*, vol. 189, pp. 128–142, Jul. 2022.
- [6] K. Takahashi, J. Igel, H. Preetz, and M. Sato, “Influence of heterogeneous soils and clutter on the performance of ground-penetrating radar for landmine detection,” *IEEE Trans. Geosci. Remote Sens.*, vol. 52, no. 6, pp. 3464–3472, Jun. 2014.
- [7] D. Edemsky, A. Popov, I. Prokopovich, and V. Garbatsevich, “Airborne ground penetrating radar, field test,” *Remote Sens.*, vol. 13, no. 4, p. 667, Feb. 2021.
- [8] M. Chang, L. Xu, X. Pang, J. Zhang, H. Li, and M. Lin, “Characteristic analysis and blind area prediction of aeromagnetic scalar gradient detection method,” *AIP Adv.*, vol. 12, no. 8, Aug. 2022, Art. no. 085211.
- [9] M. D. Wigh, M. E. Kolster, T. M. Hansen, and A. Døssing, “Classification of UXO and non-UXO from magnetic anomaly data: A case study on inversion of drone magnetic data from Rømø, Denmark,” *Geophys. J. Int.*, vol. 234, no. 2, pp. 915–932, Mar. 2023.
- [10] A. Malehmir et al., “The potential of rotary-wing UAV-based magnetic surveys for mineral exploration: A case study from central Sweden,” *Lead. Edge*, vol. 36, no. 7, pp. 552–557, Jul. 2017.
- [11] D. Macharet et al., “Autonomous aeromagnetic surveys using a fluxgate magnetometer,” *Sensors*, vol. 16, no. 12, p. 2169, Dec. 2016.
- [12] Y. Mu, X. Zhang, W. Xie, and Y. Zheng, “Automatic detection of near-surface targets for unmanned aerial vehicle (UAV) magnetic survey,” *Remote Sens.*, vol. 12, no. 3, p. 452, Feb. 2020.
- [13] J. Wang et al., “From model to algorithms: Distributed magnetic sensor system for vehicle tracking,” *IEEE Trans. Ind. Informat.*, vol. 19, no. 3, pp. 2963–2972, Mar. 2023.
- [14] M. Pérez, J. Parras, S. Zazo, I. A. Pérez Álvarez, and M. D. M. S. Lluh, “Using a deep learning algorithm to improve the results obtained in the recognition of vessels size and trajectory patterns in shallow areas based on magnetic field measurements using fluxgate sensors,” *IEEE Trans. Intell. Transp. Syst.*, vol. 23, no. 4, pp. 3472–3481, Apr. 2022.
- [15] M. E. Kolster and A. Døssing, “Scalar magnetic difference inversion applied to UAV-based UXO detection,” *Geophys. J. Int.*, vol. 224, no. 1, pp. 468–486, Jul. 2020.
- [16] Tsingtao HYH Technol. *The Unmanned Aerial Magnetic Detection System of TRU100-23[EB/OL]*. Accessed: Dec. 2024. [Online]. Available: <https://www.qd-hyh-tech.com>
- [17] *Criterion of Aeromagnetic Survey*, document DZ/T 0142-2010, Standards Press China, Beijing, China, 2010.
- [18] W. Jenkal, R. Latif, A. Toumanari, A. Dliou, O. E. B’charri, and F. M. R. Maoulainine, “An efficient algorithm of ECG signal denoising using the adaptive dual threshold filter and the discrete wavelet transform,” *Biocybern. Biomed. Eng.*, vol. 36, no. 3, pp. 499–508, 2016.
- [19] Y. Chen, Y. Cheng, and H. Liu, “Application of improved wavelet adaptive threshold de-noising algorithm in FBG demodulation,” *Optik*, vol. 132, pp. 243–248, Mar. 2017.
- [20] J. Li, C. Cheng, T. Jiang, and S. Grzybowski, “Wavelet de-noising of partial discharge signals based on genetic adaptive threshold estimation,” *IEEE Trans. Dielectr. Electr. Insul.*, vol. 19, no. 2, pp. 543–549, Apr. 2012.
- [21] Y. Shen, J. Wang, J. Shi, S. Zhao, and J. Gao, “Interpretation of signature waveform characteristics for magnetic anomaly detection using tunneling magnetoresistive sensor,” *J. Magn. Magn. Mater.*, vol. 484, pp. 164–171, Aug. 2019.